scientific reports

Check for updates

OPEN

Dirac semimetal phase and switching of band inversion in XMg$_2$Bi$_2$ (X = Ba and Sr)

Daichi Takane[1,15], Yuya Kubota[1,15], Kosuke Nakayama[1,2]✉, Tappei Kawakami[1], Kunihiko Yamauchi[3], Seigo Souma[4,5], Takemi Kato[1], Katsuaki Sugawara[1,2,4,5], Shin-ichiro Ideta[6,7,8], Kiyohisa Tanaka[6,7], Miho Kitamura[9], Koji Horiba[9,10], Hiroshi Kumigashira[11], Tamio Oguchi[12,13], Takashi Takahashi[1,4,5], Kouji Segawa[14] & Takafumi Sato[1,4,5]✉

Topological Dirac semimetals (TDSs) offer an excellent opportunity to realize outstanding physical properties distinct from those of topological insulators. Since TDSs verified so far have their own problems such as high reactivity in the atmosphere and difficulty in controlling topological phases via chemical substitution, it is highly desirable to find a new material platform of TDSs. By angle-resolved photoemission spectroscopy combined with first-principles band-structure calculations, we show that ternary compound $BaMg_2Bi_2$ is a TDS with a simple Dirac-band crossing around the Brillouin-zone center protected by the C_3 symmetry of crystal. We also found that isostructural $SrMg_2Bi_2$ is an ordinary insulator characterized by the absence of band inversion due to the reduction of spin–orbit coupling. Thus, XMg$_2$Bi$_2$ (X = Sr, Ba, etc.) serves as a useful platform to study the interplay among crystal symmetry, spin–orbit coupling, and topological phase transition around the TDS phase.

Topological Dirac semimetals (TDSs) materialize a new state of quantum matter which hosts exotic quantum phenomena such as high carrier mobility[1,2], giant linear magnetoresistance[1], and Fermi-arc-mediated surface transport[3,4]. Such physical properties are governed by the Dirac-cone energy band showing linear dispersions in all the directions in the three-dimensional (3D) momentum (k) space (k_x, k_y, and k_z) characterized by the crossing of bulk valence band (VB) and conduction band (CB) at discrete points (Dirac points) in k space. Such peculiar electronic structure is formed as a result of the band inversion due to the strong spin–orbit coupling (SOC) and the protection of band degeneracy by the time-reversal and specific crystalline symmetries. The most intriguing aspect of TDS is that it can be switched to other topological states such as quantum spin Hall states, topological insulators (TIs), Weyl semimetals, and topological superconductors[5–12]. For instance, breaking the time-reversal symmetry by an external magnetic field leads to a Weyl semimetal state possessing a pair of spin-split massless Weyl cones in the bulk and novel Fermi arcs at the surface[13,14]. Another way with a potentially high degree of freedom in manipulating the topological state is chemical substitution which may enable, e.g. to control the Dirac-cone dispersion via tuning SOC or to trigger a topological superconducting state with Majorana

[1]Department of Physics, Graduate School of Science, Tohoku University, Sendai 980-8578, Japan. [2]Precursory Research for Embryonic Science and Technology (PRESTO), Japan Science and Technology Agency (JST), Tokyo 102-0076, Japan. [3]Center for the Promotion of Interdisciplinary Education and Research, Kyoto University, Kyoto 606-8501, Japan. [4]Center for Spintronics Research Network, Tohoku University, Sendai 980-8577, Japan. [5]Advanced Institute for Materials Research (WPI-AIMR), Tohoku University, Sendai 980-8577, Japan. [6]UVSOR Synchrotron Facility, Institute for Molecular Science, Okazaki 444-8585, Japan. [7]School of Physical Sciences, The Graduate University for Advanced Studies (SOKENDAI), Okazaki 444-8585, Japan. [8]Hiroshima Synchrotron Radiation Center, Hiroshima University, Higashi-Hiroshima 739-0046, Japan. [9]Institute of Materials Structure Science, High Energy Accelerator Research Organization (KEK), Tsukuba, Ibaraki 305-0801, Japan. [10]National Institutes for Quantum and Radiological Science and Technology (QST), Sayo, Hyogo 679-5148, Japan. [11]Institute of Multidisciplinary Research for Advanced Materials (IMRAM), Tohoku University, Sendai 980-8577, Japan. [12]Center for Spintronics Research Network, Osaka University, Toyonaka 560-8531, Japan. [13]Institute of Scientific and Industrial Research, Osaka University, Ibaraki, Osaka 567-0047, Japan. [14]Department of Physics, Kyoto Sangyo University, Kyoto 603-8555, Japan. [15]These authors contributed equally: Daichi Takane and Yuya Kubota. ✉email: k.nakayama@arpes.phys.tohoku.ac.jp; t-sato@arpes.phys.tohoku.ac.jp

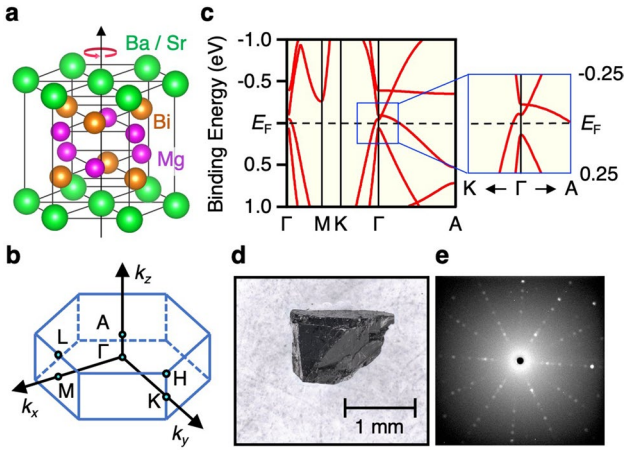

Figure 1. (**a**,**b**) Crystal structure and bulk hexagonal BZ of XMg_2Bi_2 (X = Sr and Ba), respectively. (**c**) Calculated band structure of $BaMg_2Bi_2$ along high-symmetry lines in bulk BZ obtained from the first-principles band-structure calculations, and its expanded view around the Dirac point (right panel). (**d**) Photograph of $BaMg_2Bi_2$ single crystal. (**e**) X-ray Laue backscattering image of $BaMg_2Bi_2$ obtained for the (0001) surface.

fermions by carrier doping. Angle-resolved photoemission spectroscopy (ARPES) has played a pivotal role in clarifying TDSs by directly visualizing the bulk Dirac-cone band, as demonstrated in Na_3Bi, Cd_3As_2, and α-Sn/InSb(111)[5,7,15–18] which host Dirac-cone bands protected by the rotational symmetry. Despite many theoretical predictions for TDS candidates[19–29], experimental investigations *hitherto* performed on TDSs are mainly focused on these prototypical TDSs, which, however, have inherent problems such as high reactivity in the atmosphere and/or difficulty of chemical substitution of elements in crystals. Thus, it is highly desirable to explore new TDS materials which overcome such difficulties.

Recently, it was proposed that a ternary compound $BaMg_2Bi_2$ is a 3D TDS[30] from the automated construction of Wannier functions and high-throughput screening out of non-topological materials. In $BaMg_2Bi_2$ crystal, Ba atoms can be easily replaced with other elements, and its general chemical composition is expressed as XMg_2Bi_2 where X represents alkaline earth or rare earth metal (Ca, Sr, Ba, Yb, Eu, etc.)[31–35]. XMg_2Bi_2 crystalizes in the $CaAl_2Si_2$-type structure (space group of $P\bar{3}m1$, No. 164[36] which has the C_3 rotational symmetry with respect to the c-axis (Fig. 1a; the Brillouin zone (BZ) is shown in Fig. 1b). Our first-principles band-structure calculations including SOC shown in Fig. 1c reveal that $BaMg_2Bi_2$ possesses a Dirac cone close to the Fermi level (E_F) along the ΓA line of bulk BZ (Fig. 1b) due to the bulk-band inversion and the protection by the C_3 symmetry, consistent with the previous calculation[30]. The predicted simple band structure with no E_F crossings of other bands with topologically trivial origin makes $BaMg_2Bi_2$ an excellent system to search for exotic properties associated with bulk Dirac fermions. Moreover, the XMg_2Bi_2 family has a high potential to realize different types of topological states. For example, controlling the SOC by replacing the X element and breaking the crystal symmetry e.g. by applying pressure may trigger the topological phase transition to other phases such as TI and ordinary insulator phases[30,37]. Despite such interesting proposals, the electronic states of XMg_2Bi_2 family have been scarcely investigated. It is thus urgently required to clarify its fundamental band structure.

In this work, we report high-resolution angle-resolved photoemission spectroscopy (ARPES) of XMg_2Bi_2 (X = Sr and Ba) single crystals. By utilizing energy-tunable soft-X-ray (SX) and vacuum ultraviolet (VUV) photons from synchrotron radiation, we experimentally established the electronic structure of $BaMg_2Bi_2$ over the 3D bulk BZ and found an evidence for the existence of bulk Dirac fermions characterized by the band touching of bulk VB and CB. In sharp contrast, we found a bulk-band gap in $SrMg_2Bi_2$ suggestive of its ordinary insulator nature. We discuss the obtained results in relation to the band-structure calculation, SOC, and topological phase transition.

Results and discussion

Samples and experimental. XMg_2Bi_2 single crystals with typical size of $2 \times 2 \times 1$ mm^3 (see Fig. 1d) were synthesized by the self-flux method (for details, see "Methods"). ARPES measurements were performed with micro-focused VUV synchrotron light at BL28 in Photon Factory and BL5U in UVSOR, and also with SX photons at BL2 in Photon Factory. Samples were cleaved in situ along the (0001) plane of the hexagonal crystal in an ultrahigh vacuum of 1×10^{-10} Torr. Prior to ARPES measurements, the crystal orientation was determined by the X-ray Laue backscattering measurements which signify clear six-fold symmetric diffraction spots consistent with the (0001) cleaved plane, as shown in Fig. 1e.

Valence-band structure of $BaMg_2Bi_2$. We at first discuss the overall electronic structure of $BaMg_2Bi_2$. Figure 2a displays the energy distribution curve in a wide energy range measured at the photon energy ($h\nu$) of 500 eV. One can recognize several core-level peaks which are assigned to the Ba (5s, 5p), Mg (2p), and Bi (5p, 5d) orbitals. The sharp spectral feature and the absence of core-level peaks from other elements confirm the clean

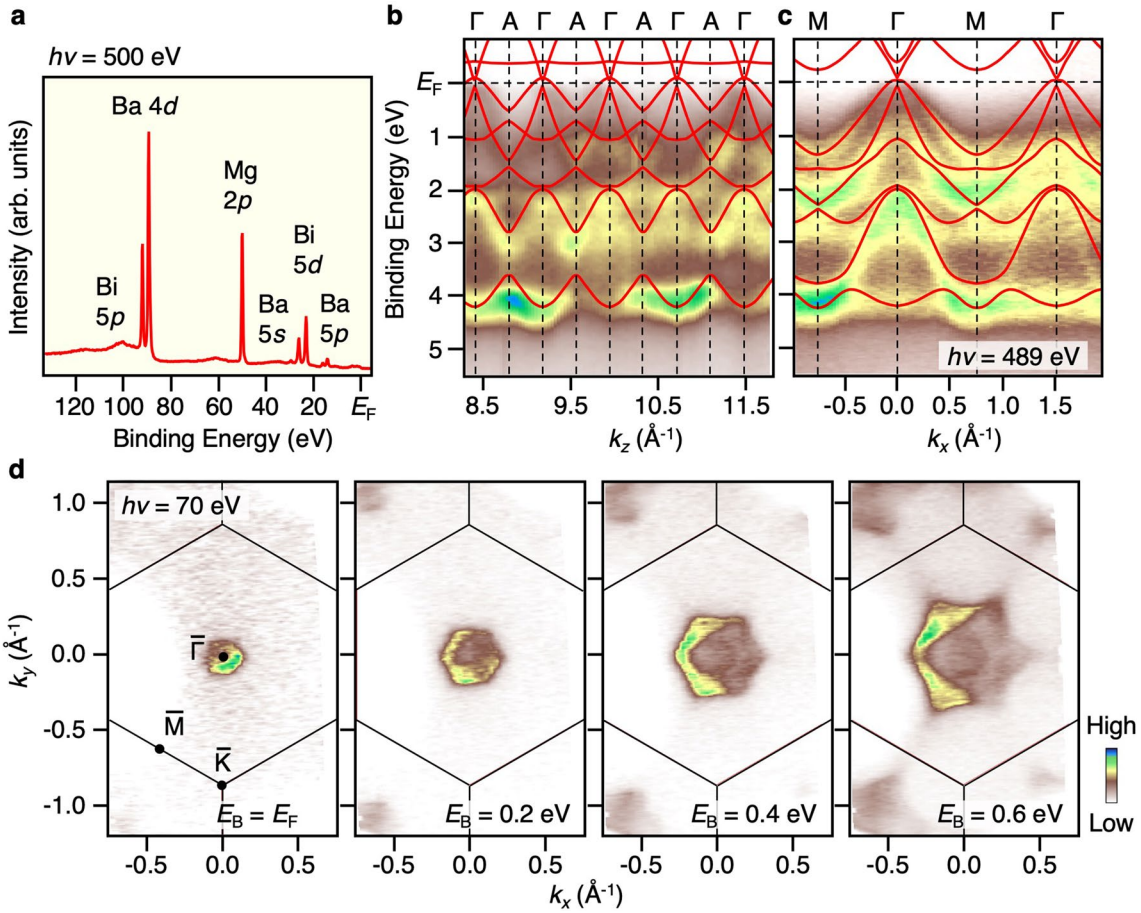

Figure 2. (**a**) Energy distribution curve of $BaMg_2Bi_2$ in a wide binding-energy (E_B) range measured at $h\nu = 500$ eV. (**b**) ARPES intensity of $BaMg_2Bi_2$ measured at $T = 40$ K along the ΓA cut by varying $h\nu$ from 250 to 522 eV, together with the calculated band structure (red curve). The inner potential was estimated to be $V_0 = 15.0$ eV from the periodicity of out-of-plane band dispersion. (**c**) ARPES intensity along the $\overline{\Gamma M}$ cut measured at $h\nu = 489$ eV. Calculated band structure along the ΓM cut is also overlaid. (**d**) Plots of ARPES intensity as a function of two-dimensional wave vector (k_x and k_y) at representative E_B slices ($E_B = 0$, 0.2, 0.4, and 0.6 eV) measured at $h\nu = 70$ eV for $BaMg_2Bi_2$.

sample surface. Besides the core levels, one can find a weak feature near E_F originating from the VB composed mainly of the Bi 6*p* orbitals. To determine the 3D bulk electronic states, we performed ARPES measurements at the normal-emission setup with varying $h\nu$ in the SX region (250–522 eV). To visualize the bulk band in 3D k space, it is useful to use bulk-sensitive SX photons, because the increase of photoelectron mean-free path compared to VUV photons reduces the intrinsic uncertainty of the out-of-plane wave vector k_z through the Heisenberg's uncertainty principle and as a result allows the accurate 3D band mapping. Figure 2b shows the obtained VB dispersion along the wave vector perpendicular to the sample surface (k_z). One can recognize some energy bands displaying a finite k_z dispersion, e.g., at the binding energies E_B's of E_F-1.5 eV, 2–3 eV, and 3.7–4.3 eV. The observed band dispersions well follow the periodicity of the bulk BZ; for example, the near-E_F band appears to have the top and bottom of dispersion at Γ and A points, respectively, consistent with the bulk-band calculations including SOC (red curves). A good matching of periodic oscillation in the band dispersion between the experiment and calculation is seen in the entire E_B region, showing their bulk-origin nature.

Since the VB has the top of dispersion around the Γ point of bulk BZ, next we carried out ARPES measurements along the in-plane k_x cut crossing the Γ point (ΓM cut), as shown in Fig. 2c. One can recognize several bands whose energy dispersion is reproduced semi-quantitatively by the band calculation along the ΓM cut, suggesting no discernible band-mass renormalization, indicative of a weak electron correlation in $BaMg_2Bi_2$. One can also see two hole bands which rapidly disperse toward E_F with approaching the Γ point. The outer one appears to cross E_F and forms a hole pocket centered at the Γ point. To visualize the topmost VB more clearly, we plot in Fig. 2d the ARPES intensity as a function of in-plane wave vector, k_x and k_y, at selected E_B slices ($E_B = E_F$, 0.2, 0.4, 0.6 eV) at $k_z \sim 0$ (in reduced BZ scheme; $k_z = 7 \times 2\pi/c$ in extended BZ), measured with VUV photons ($h\nu = 70$ eV) that achieve higher energy and k resolution. At $E_B = E_F$, one can clearly see a circular Fermi surface centered at the Γ point. This Fermi surface follows the periodicity of hexagonal BZ (for details, see Supplementary Fig. S1). With increasing E_B, the circular intensity pattern gradually expands and shows a stronger hexagonal deformation, signifying that the topmost VB forms a hole pocket, consistent with the positive sign of Hall coefficient in our sample (see Supplementary Fig. S2). Taking into account the sizable k_z dispersion of the topmost

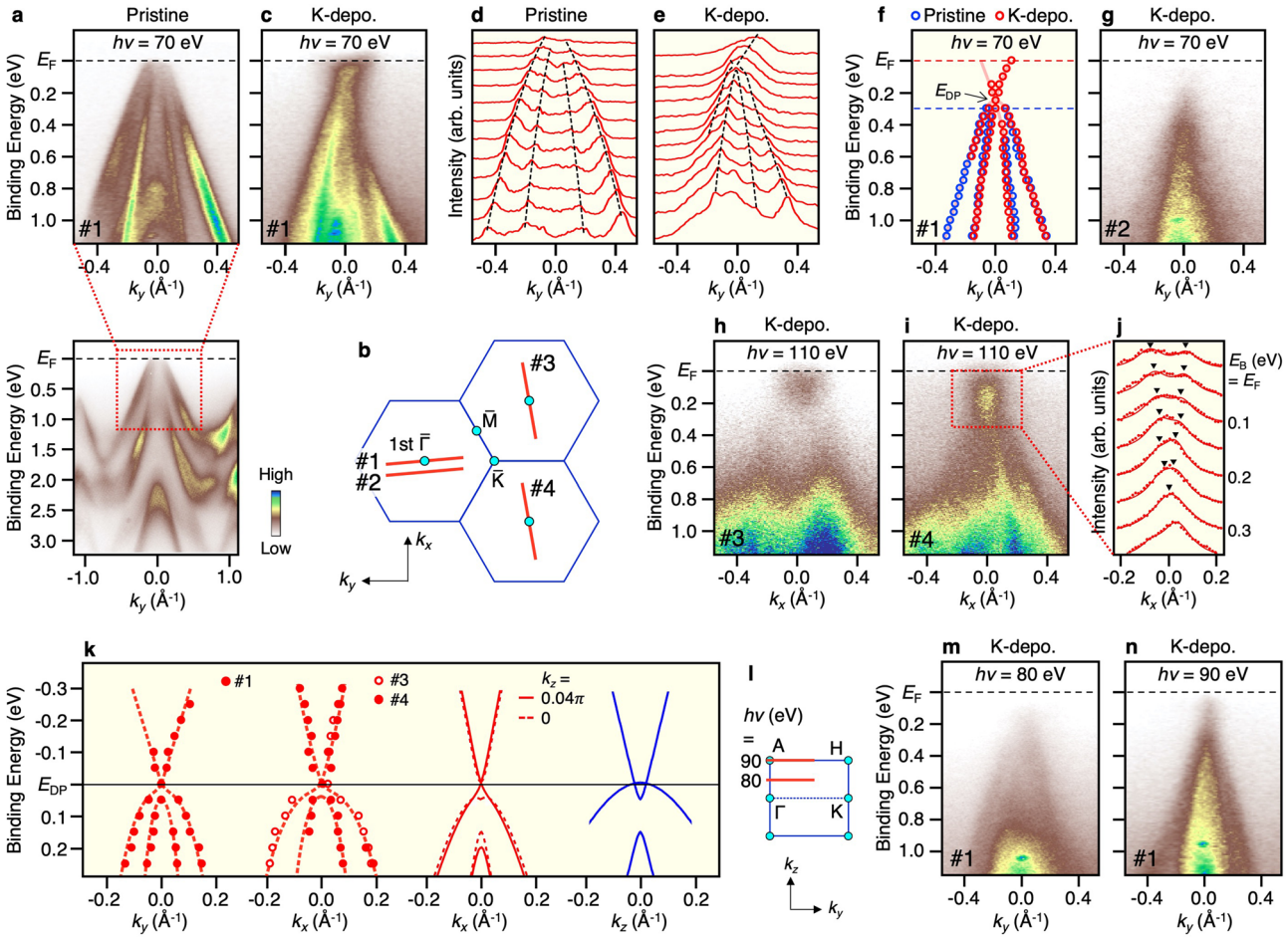

Figure 3. (**a**) VB ARPES intensity (bottom panel) and expanded image in the vicinity of E_F (top panel) for $BaMg_2Bi_2$ measured nearly along the ΓK cut at $h\nu = 70$ eV. (**b**) Brillouin zone of $BaMg_2Bi_2$ in the k_x–k_y plane together with k cuts where the ARPES data shown in (**c**) (cut #1), (**g**) (cut #2), (**h**) (cut #3), and (**i**) (cut #4) were obtained. (**c**) ARPES intensity near E_F measured along cut #1 after K deposition onto the surface of $BaMg_2Bi_2$. (**d**,**e**) MDCs at several E_B's (E_F-1.1 eV) corresponding to the ARPES intensity of (**a**) and (**b**), respectively. Dashed curves are a guide to the eyes to trace the band dispersion. (**f**) Experimental band dispersions along cut #1 for pristine and K-deposited $BaMg_2Bi_2$, obtained by tracing the peak position of MDCs in (**d**) and (**e**). Band dispersion for pristine sample is shifted downward by 0.3 eV with respect to that of K-deposited counterpart to align the energy position of the Dirac point. (**g**) ARPES intensity measured along cut #2 for K-deposited $BaMg_2Bi_2$. (**h**,**i**) ARPES intensity measured along cuts #3 and #4, respectively, for K-deposited $BaMg_2Bi_2$. (**j**) MDCs in the area enclosed by red rectangle in (**i**). (**k**) Experimental band dispersion (circles and dashed curves) obtained from the MDC analyses along cuts #1, #3, and #4, compared with the calculated band dispersion along the k_x cut at $k_z = 0$ (ΓM cut; red dashed curve) and 0.04 Å^{-1} (k cut crossing the Dirac point; red solid curve), and with that along the k_z axis (ΓA cut; blue curves). Experimental and calculated band dispersions are aligned in energy with respect to the Dirac point. (**l**) Brillouin zone of $BaMg_2Bi_2$ in the k_y–k_z plane together with k cuts where ARPES measurements shown in panels (**m**) and (**n**) were performed. (**m**,**n**) ARPES intensity for K-deposited $BaMg_2Bi_2$ measured at $h\nu = 80$ eV and 90 eV, respectively.

VB (Fig. 2b), it is suggested that the hole pocket has the 3D character. By assuming an isotropic spherical shape, we have estimated the hole carrier concentration to be 7×10^{18} cm^{-3}. This value is in rough agreement with the value estimated from the Hall coefficient (2.4×10^{18} cm^{-3} at $T = 50$ K; for details, see Supplementary Sect. 2 of Supplementary Information), suggesting that the ARPES data reflect intrinsic bulk properties.

Now that the overall VB dispersion is established, we present the near-E_F band structure to examine the existence of bulk Dirac fermions. Figure 3a shows the ARPES intensity (bottom panel) and its expanded view in the vicinity of E_F (top panel), measured almost along the ΓK (k_y) cut (cut #1 in Fig. 3b) at $h\nu = 70$ eV. One can see linearly dispersive inner and outer hole bands, and the latter crosses E_F. Since hole carriers are doped into the crystal due to the slight off-stoichiometry of chemical composition, we were unable to see the bulk CB on the bare surface. To search for a possible band touching of VB and CB predicted in the calculation, we deposited K atoms onto the surface of $BaMg_2Bi_2$ in ultrahigh vacuum. One can clearly see in Fig. 3c that the hole bands in K-deposited $BaMg_2Bi_2$ are shifted downward as a whole by ~0.3 eV with respect to those in pristine $BaMg_2Bi_2$ due to the electron doping to the surface. Intriguingly, VB in the negative k_y region appears to almost continuously disperse across $k = 0$ and cross E_F at positive k_y, without losing its intensity at $k_y = 0$, suggestive of the absence of

band gap. Taking into account that the linearly dispersive VB at positive k_y shows a weaker intensity due to the dipole matrix-element effect of photoelectron intensity, together with the expectation that the band dispersion is symmetric with respect to $k_y = 0$, it is suggested that the VB and CB touch each other at the Γ point and forms the Dirac-cone-like dispersion. To corroborate the band touching, we show in Fig. 3d,e the momentum distribution curves (MDCs) corresponding to the ARPES intensity of Fig. 3a,c, respectively. One can see that, in K-deposited $BaMg_2Bi_2$ (Fig. 3e), the peak for the bulk VB is smoothly connected to that for the bulk CB without obvious discontinuity around the Γ point, supporting the absence of an energy gap. This is also visualized by the experimental band dispersion obtained by tracing the peak position of MDCs shown in Fig. 3f. The band touching only at a single k point in the k_x-k_y plane (i.e., the $\overline{\Gamma}$ point of the surface Brillouin zone) is confirmed by the ARPES intensity measured along the off-$\overline{\Gamma}$ cut (cut #2 in Fig. 3b) in Fig. 3g that signifies the apparent absence of CB due to an energy separation between the CB and the VB, supporting the cone-shaped band dispersion. To further support this conclusion, we have carried out ARPES measurements with different experimental conditions. Figure 3h,i show the representative ARPES intensity after the K deposition on the surface of $BaMg_2Bi_2$ obtained by another cleaving, measured at $h\nu = 110$ eV nearly along the ΓM cut (#3 and #4, respectively, in Fig. 3b) thus with different light polarization with respect to the sample surface. While the distribution of ARPES intensity is different from that of Fig. 3c (note that somewhat fuzzy character of the ARPES spectrum along the ΓM cut is attributed to the matrix-element effect of photoelectron intensity), these intensity patterns commonly show that CB is located rightly above the VB without a band-gap opening. As shown in Fig. 3j, the plot of MDCs in the $E_B = 0$–0.35 eV region of Fig. 3i reveals two broad peaks at $E_B = E_F$ (triangles) whose k separation becomes gradually smaller with increasing E_B, and the two peaks eventually merge into a single peak at $E_B = 0.3$ eV. This signifies the existence of V-shaped CB. We have experimentally determined the energy position of VB and CB from numerical fittings of MDCs in Fig. 3c,h,i and found that outer hole band appears to touch the CB at the Γ point within our experimental uncertainty, as shown in the two panels on the left side of Fig. 3k. The band dispersion determined by ARPES shows an overall agreement with the calculated band dispersions along the ΓM cut ($k_z = 0$; dashed curves, slightly away from the Dirac point) and off-ΓM cut ($k_z = 0.04$ Å^{-1}; solid curves, passing through the Dirac point) as shown in the second panel from the right in Fig. 3k. As shown in the right panel of Fig. 3k, the calculated Dirac points exist not exactly at the Γ point but slightly (by 0.04 Å^{-1}) away from the Γ point along the ΓA cut. By taking into account the finite k_z broadening (0.1–0.2 Å^{-1}, estimated from the photoelectron escape depth) which is wider than the k separation between adjacent Dirac points, the present ARPES data would reflect the band dispersion integrated over the k_z region involving two Dirac points. Thus, although it is difficult to resolve each Dirac point due to the inevitable k_z broadening effect, the overall agreement between the experimental and calculated band dispersions is consistent with the existence of Dirac points around the Γ point, and therefore supportive of the TDS nature of $BaMg_2Bi_2$. To support the 3D nature of the band touching, we show in Fig. 3m,n the ARPES intensity measured with $h\nu = 80$ and 90 eV which correspond to $k_z \sim 0.5\pi$ (between AH and ΓK cut) and π (AH cut), respectively (Fig. 3l). One can recognize that the CB seen at $h\nu = 70$ eV (along the ΓK cut; Fig. 3c) is absent for both $h\nu = 80$ and 90 eV because it moves upward and enters the unoccupied region, suggesting that the band touching occurs in a particular k_z point ($k_z \sim 0$) in the 3D Brillouin zone, indicative of the overall 3D cone-shaped nature of the bulk band dispersion. This also suggests that the influence of K-deposition-induced electron doping extends into the bulk region, so that the quantized two-dimensional CB, as observed in semiconductor surfaces[38], is not formed in K-deposited $BaMg_2Bi_2$.

Switching of band inversion. Next we address an important question whether or not the electronic structure of isostructural $SrMg_2Bi_2$ is similar to that of $BaMg_2Bi_2$. Figure 4a displays the ARPES intensity along the ΓM cut for $SrMg_2Bi_2$ measured with SX photons ($h\nu = 489$ eV). One can recognize qualitatively similar VB dispersions to those of $BaMg_2Bi_2$ (Fig. 2c), for example, three prominent hole bands centered at the Γ point and relatively flat band at around 4–4.5 eV, are clearly observed, while there exist some quantitative differences such as a slight downward shift of the flat band in $SrMg_2Bi_2$ relative to $BaMg_2Bi_2$. The topmost hole band crosses E_F in $SrMg_2Bi_2$, as better visualized in the high-resolution ARPES data in the vicinity of E_F shown in Fig. 4b measured with VUV photons which probe the Γ point ($h\nu = 80$ eV). To examine the possible band touching of VB and CB, we deposited K atoms on the surface of $SrMg_2Bi_2$ as in the case of $BaMg_2Bi_2$. As shown in Fig. 4c, although the hole bands shift downward after K deposition, surprisingly, the spectral weight associated with the CB is absent and no Fermi-edge cut-off is observed, in stark contrast to the case of K-deposited $BaMg_2Bi_2$ (Fig. 3c,h,i). This contrast behavior is clearly seen in the EDCs at the Γ point (red curves in Fig. 4c,d). The absence of spectral weight above the VB top cannot be explained in terms of the existence of bulk CB with suppressed intensity, because the photoionization cross-section of Ba 6*s* and Sr 5*s* orbitals that dominantly contribute to the CB[30] is almost equal to each other at $h\nu = 70$–80 eV[39] (also see Supplementary Fig. S3 which shows the absence of the CB-derived intensity in the ARPES data measured along different k cuts or at different $h\nu$'s). It is thus concluded that an intrinsic band gap opens in $SrMg_2Bi_2$. This suggests the occurrence of topological phase transition from the TDS state to the insulating phase upon gradually replacing Ba with Sr.

Now we discuss the origin of observed drastic difference in the near-E_F band structure between $BaMg_2Bi_2$ and $SrMg_2Bi_2$. According to the calculation[30], the existence of bulk Dirac-cone band in $BaMg_2Bi_2$ is associated with the protection of band degeneracy along the ΓA line by C_3 rotational symmetry of the crystal, besides the band inversion of bulk VB and CB with different parities. Taking into account these conditions, one can think of two possibilities to account for the transition to the bulk insulating phase upon replacement of Ba with Sr. One is a transition to the TI phase caused by the C_3-symmtery breaking, and another is transformation into an ordinary insulator by dissolving the band inversion. The former possibility is ruled out because (i) $SrMg_2Bi_2$ has the same space group as $BaMg_2Bi_2$ so that the C_3 symmetry is preserved, and (ii) no evidence for the topological Dirac-cone surface state was found within the bulk band gap. One may think that crystal imperfections such as

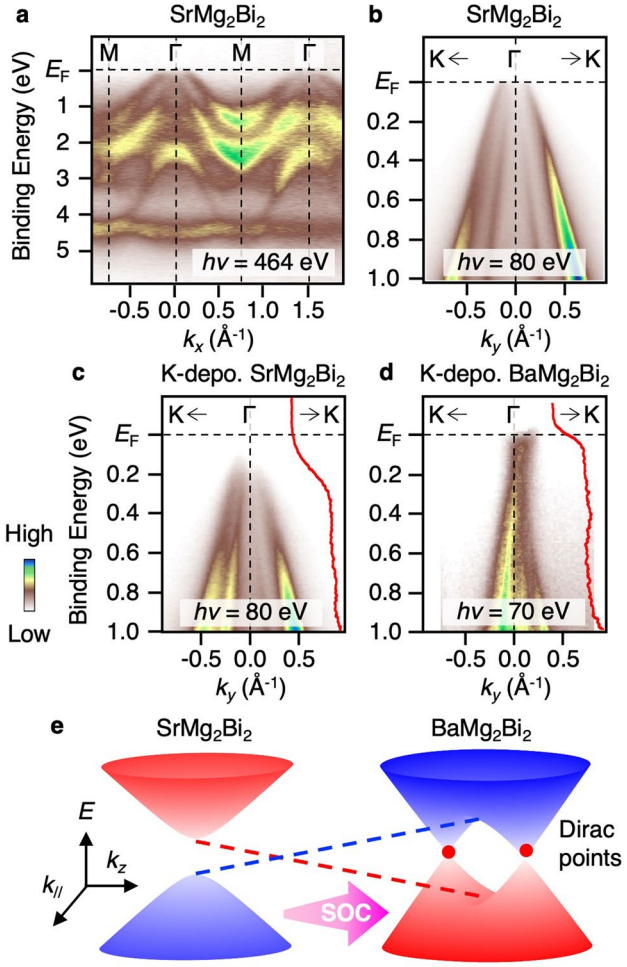

Figure 4. (**a**) VB ARPES intensity of $SrMg_2Bi_2$ measured at $T = 40$ K along the ΓM cut at $h\nu = 489$ eV. (**b**,**c**) ARPES intensity in the vicinity of E_F of $SrMg_2Bi_2$ before and after K deposition, respectively, measured almost along the ΓK cut (cut #1 in Fig. 3b) at $h\nu = 80$ eV. (**d**) ARPES intensity for K-deposited $BaMg_2Bi_2$ (same as Fig. 3c). EDCs at the Γ point are shown in (**c**) and (**d**). (**e**) Schematic band diagram of XMg_2Bi_2 suggested from the ARPES results.

disorders, defects, vacancies, and/or strain may break the C_3 symmetry. To break the C_3 symmetry globally and open a large Dirac gap throughout the crystal, a substantial amount of disorders, defects, and/or vacancies must be present in our $SrMg_2Bi_2$ crystals. Local symmetry breaking by a small amount of imperfections unlikely causes a clear gap opening in the ARPES spectrum because ARPES reflects information of photoelectron signal emitted from a wide area over few-tens of micrometers. While such substantial disorders, defects, and/or vacancies may lead to significant spectral broadening in $SrMg_2Bi_2$, our ARPES results indicate that the sharpness of ARPES spectrum is comparable between $SrMg_2Bi_2$ and $BaMg_2Bi_2$ (e.g., compare Fig. 4a and Supplementary Fig. S1b). Therefore, a clear gap opening observed only in $SrMg_2Bi_2$ is unlikely triggered by disorders, defects, and/or vacancies. Also, it is unlikely that accidentally introduced strain in the crystal could globally and reproducibly break the C_3 symmetry (note that we have confirmed the reproducibility of the gap opening for different crystals). Therefore, the crystal imperfection would not be a main cause of the observed gap in $SrMg_2Bi_2$. Thus, the latter possibility, transformation into an ordinary insulator, is likely the case. This conclusion is reasonable because the replacement of Ba with lighter Sr reduces the strength of SOC and may dissolve the band inversion (Fig. 4e) (note that $SrMg_2Bi_2$ can be either a trivial insulator or a TDS with a small band inversion by our calculations, depending on the approximation used, likely because $SrMg_2Bi_2$ is in the vicinity of the topological phase transition; for details, see Supplementary Fig. S5).

Finally, we compare the TDS characteristics of $BaMg_2Bi_2$ with other well-known TDSs, Na_3Bi and Cd_3As_2[5,7,15–17]. These TDSs share several common features, for example, the Dirac-cone band is protected by the rotational (C_3 or C_4) symmetry of crystal and the band inversion is associated with the *s* orbital of CB and *p* orbital of VB. We found that the Fermi velocity of $BaMg_2Bi_2$ (4.2 eV Å) is comparable to that of Na_3Bi (2.4–2.8 eV Å)[5] and Cd_3As_2 (8.47–9.8 eV Å)[16,17], implying a potential to achieve a high mobility in $BaMg_2Bi_2$. Also, the SOC of $BaMg_2Bi_2$ is as strong as that of Na_3Bi and Cd_3As_2 because the Dirac-cone band is formed by the orbital of heavy elements, i.e. Bi 6*p* and Ba 6*s*. Regarding the robustness of crystal against the exposure to the air, $BaMg_2Bi_2$ and Cd_3As_2 have an advantage over Na_3Bi, because Na_3Bi is known to be very unstable in the

atmosphere. It is noted that our XMg$_2$Bi$_2$ crystals were stable for at least 1 week in the atmosphere. The robustness is important for reliable measurements of physical properties as well as applications to practical devices. Most intriguing aspect of BaMg$_2$Bi$_2$ compared to other TDSs is that chemical substation can be carried out with ease; e.g. Ba atoms can be completely replaced with other elements in BaMg$_2$Bi$_2$ whereas only partial Cd or As can be replaced with other elements in Cd$_3$As$_2$[40,41] and even partial substitution is hard to be done in Na$_3$Bi. These characteristics make the XMg$_2$Bi$_2$ system an excellent platform to investigate the topological phase transition starting from the TDS phase.

In conclusion, we have reported the ARPES results of XMg$_2$Bi$_2$ (X = Sr and Ba). Through the band-structure mapping in the 3D BZ by utilizing energy-tunable SX and VUV photons, we revealed that the electronic structure of BaMg$_2$Bi$_2$ is characterized by the touching of bulk VB and CB around the Γ point, supporting its TDS nature. On the other hand, a sizable bulk band gap observed in SrMg$_2$Bi$_2$ suggests its ordinary insulator nature. We concluded that the chemical substitution in XMg$_2$Bi$_2$ works as an effective means to control the topological phase. The present result paves a pathway toward understanding the interplay among SOC, crystal symmetry, and topological phase transition in TDSs.

Methods

Sample preparation. XMg$_2$Bi$_2$ single crystals were synthesized by the self-flux method. The purity of starting materials is > 99% for Sr and Ba, > 99.9% for Mg, and 99.999% for Bi, respectively. Those materials were loaded in an alumina crucible with the molar ratio of X:Mg:Bi = 1:4:6 and the heat treatment was performed in a sealed quartz tube. The growth process is essentially the same as the previous report[32], including removal of the flux with a centrifuge at a high temperature of ~ 650 °C. A 2θ–θ X-ray diffraction scan confirmed that the growth facet is (0001) plane and the obtained c-axis lattice constant is consistent with that of the target phase.

ARPES experiments. VUV-ARPES measurements with micro-focused synchrotron light were performed with a DA30 electron analyzer at BL28 in Photon Factory and also with a MBS-A1 analyzer at BL5U in UVSOR. We used circularly/linearly polarized light of 36–200 eV. SX-ARPES measurements were performed with a SES2002 analyzer at BL2 in Photon Factory with 230–600 eV photons with horizontal linear polarization. The energy resolutions for VUV- and SX-ARPES measurements were set to be 10–30 meV and 150 meV, respectively. Samples were cleaved in situ along the (0001) plane of the hexagonal crystal in an ultrahigh vacuum of 1×10^{-10} Torr, and kept at T = 4.5–40 K during the measurements.

Calculations. First-principles band-structure calculations shown in Figs. 1, 2 and 3 were carried out by using the Quantum Espresso code package[42] with generalized gradient approximation (GGA)[43]. Ultrasoft pseudopotential was used and the SOC was included in the calculations. The plane-wave cutoff energy and the k-point mesh were set to be 70 Ry and $8 \times 8 \times 8$, respectively. We have also performed band-structure calculations by using a projector augmented wave method implemented in Vienna Ab initio Simulation Package (VASP) code[44] with GGA, local-density approximation (LDA), and Heyd–Scuseria–Ernzerhof (HSE06) hybrid functional, as shown in Supplementary Fig. S5.

Data availability

The data that support the findings of this study are available from the corresponding authors upon reasonable request.

Received: 23 August 2021; Accepted: 26 October 2021
Published online: 09 November 2021

References

1. Liang, T. *et al.* Ultrahigh mobility and giant magnetoresistance in the Dirac semimetal Cd$_3$As$_2$. *Nat. Mater.* **14**, 280 (2014).
2. Feng, J. *et al.* Large linear magnetoresistance in Dirac semimetal Cd$_3$As$_2$ with Fermi surfaces close to the Dirac points. *Phys. Rev. B* **92**, 081306(R) (2015).
3. Potter, A. C., Kimchi, I. & Vishwanath, A. Quantum oscillations from surface Fermi arcs in Weyl and Dirac semimetals. *Nat. Commun.* **5**, 5161 (2014).
4. Moll, P. J. W. *et al.* Transport evidence for Fermi-arc-mediated chirality transfer in the Dirac semimetal Cd$_3$As$_2$. *Nature* **535**, 266 (2016).
5. Liu, Z. K. *et al.* Discovery of a three-dimensional topological Dirac semimetal, Na$_3$Bi. *Science* **343**, 864 (2014).
6. Yang, B.-J. & Nagaosa, N. Classification of stable three-dimensional Dirac semimetals with nontrivial topology. *Nat. Commun.* **5**, 4898 (2014).
7. Wang, Z., Weng, H., Wu, Q., Dai, X. & Fang, Z. Three-dimensional Dirac semimetal and quantum transport in Cd$_3$As$_2$. *Phys. Rev. B* **88**, 125427 (2013).
8. Uchida, M. *et al.* Quantum Hall states observed in thin films of Dirac semimetal Cd$_3$As$_2$. *Nat. Commun.* **8**, 2274 (2017).
9. Schumann, T. *et al.* Observation of the quantum hall effect in confined films of the three-dimensional Dirac semimetal Cd$_3$As$_2$. *Phys. Rev. Lett.* **120**, 016801 (2018).
10. Kobayashi, S. & Sato, M. Topological superconductivity in Dirac semimetals. *Phys. Rev. Lett.* **115**, 187001 (2015).
11. Narayan, A., Sante, D. D., Picozzi, S. & Sanvito, S. Topological tuning in three-dimensional Dirac semimetals. *Phys. Rev. Lett.* **113**, 256403 (2014).
12. Zhang, D., Wang, H., Ruan, J., Yao, G. & Zhang, H. Engineering topological phases in the Luttinger semimetal α-Sn. *Phys. Rev. B* **97**, 195139 (2018).
13. Xiong, J. *et al.* Evidence for the chiral anomaly in the Dirac semimetal Na$_3$Bi. *Science* **350**, 413–416 (2015).
14. Zhang, C. *et al.* Quantum Hall effect based on Weyl orbits in Cd$_3$As$_2$. *Nature* **565**, 331–336 (2019).
15. Wang, Z. *et al.* Dirac semimetal and topological phase transitions in A_3Bi (A = Na, K, Rb). *Phys. Rev. B* **85**, 195320 (2012).

16. Neupane, M. *et al.* Observation of a three-dimensional topological Dirac semimetal phase in high-mobility Cd_3As_2. *Nat. Commun.* **5**, 3786 (2014).
17. Liu, Z. K. *et al.* A stable three-dimensional topological Dirac semimetal Cd_3As_2. *Nat. Mater.* **13**, 677 (2014).
18. Xu, C.-Z. *et al.* Elemental topological Dirac semimetal: α-Sn on InSb(111). *Phys. Rev. Lett.* **118**, 146402 (2017).
19. Kariyado, T. & Ogata, M. Three-dimensional Dirac electrons at the fermi energy in cubic inverse perovskites: Ca_3PbO and its family. *J. Phys. Soc. Jpn.* **80**, 083704 (2011).
20. Gibson, Q. D. *et al.* Three-dimensional Dirac semimetals: Design principles and predictions of new materials. *Phys. Rev. B* **91**, 205128 (2015).
21. Yu, R., Weng, H., Fang, Z., Dai, X. & Hu, X. Topological node-line semimetal and Dirac semimetal state in antiperovskite Cu_3PdN. *Phys. Rev. Lett.* **115**, 036807 (2015).
22. Barman, C. K., Mondal, C., Pathak, B. & Alam, A. Symmetry-driven topological phases in *X*AgBi (*X* = Ba, Sr): An ab initio hybrid functional calculation. *Phys. Rev. Mater.* **4**, 084201 (2020).
23. Mardanya, S. *et al.* Prediction of threefold fermions in a nearly ideal Dirac semimetal BaAgAs. *Phys. Rev. Mater.* **3**, 071201(R) (2019).
24. Du, Y. *et al.* Dirac and weyl semimetal in *XY*Bi (*X* = Ba, Eu; *Y* = Cu, Ag and Au). *Sci. Rep.* **5**, 14423 (2015).
25. Le, C. *et al.* Three-dimensional topological critical Dirac semimetal in *A*MgBi (*A* = K, Rb, Cs). *J. Phys. Rev. B* **96**, 115121 (2017).
26. Le, C. *et al.* Dirac semimetal in β-CuI without surface Fermi arcs. *Proc. Natl. Acad. Sci. USA* **115**, 8311 (2018).
27. Wu, Q. S., Piveteau, C., Song, Z. & Yazyev, O. V. $MgTa_2N_3$: A reference Dirac semimetal. *Phys. Rev. B* **98**, 081115(R) (2018).
28. Mondal, C., Barman, C. K., Alam, A. & Pathak, B. Broken symmetry driven phase transitions from a topological semimetal to a gapped topological phase in SrAgAs. *Phys. Rev. B* **99**, 205112 (2019).
29. Huang, H., Jin, K.-H. & Liu, F. Alloy engineering of topological semimetal phase transition in $MgTa_{2-x}Nb_xN_3$. *Phys. Rev. Lett.* **120**, 136403 (2018).
30. Zhang, Z. *et al.* High-throughput screening and automated processing toward novel topological insulators. *J. Phys. Chem. Lett.* **9**, 6224 (2018).
31. Pakhira, S., Tanatar, M. A. & Johnston, D. C. Magnetic, thermal, and electronic-transport properties of $EuMg_2Bi_2$ single crystals. *Phys. Rev. B* **101**, 214407 (2020).
32. May, A. F., McGuire, M. A., Singh, D. J., Custelcean, R. & Jellison, G. E. Jr. Structure and properties of single crystalline $CaMg_2Bi_2$, $EuMg_2Bi_2$, and $YbMg_2Bi_2$. *Inorg. Chem.* **50**, 11127 (2011).
33. Ramirez, D., Gallagher, A., Baumbach, R. & Siegrist, T. Synthesis and characterization of the divalent samarium Zintl-phases $SmMg_2Bi_2$ and $SmMg_2Sb_2$. *J. Solid. State. Chem.* **231**, 217 (2015).
34. May, A. F. *et al.* Thermoelectric transport properties of $CaMg_2Bi_2$, $EuMg_2Bi_2$, and $YbMg_2Bi_2$. *Phys. Rev. B* **85**, 035202 (2012).
35. Marshall, M. *et al.* Magnetic and electronic structures of antiferromagnetic topological material candidate $EuMg_2Bi_2$. *J. Appl. Phys.* **129**, 035106 (2021).
36. Deller, K. & Eisenmann, B. Erdalkali-Element(V)-Verbindungen AMg_2B_2. *Zeitschrift für Naturforschung B* **32**, 612 (1977).
37. Petrova, E. K., Silkin, I. V., Koroteev, Y. M. & Chulkov, E. V. Effect of deformation on the electronic structure and topological properties of the $A^{II}Mg_2Bi_2$ (A^{II} = Mg, Ca, Sr, Ba) compounds. *JETP Lett.* **105**, 502 (2017).
38. Santander-Syro, A. F. *et al.* Two-dimensional electron gas with universal subbands at the surface of $SrTiO_3$. *Nature* **469**, 189 (2011).
39. Yeh, J. J. & Lindau, I. Atomic subshell photoionization cross sections and asymmetry parameters: $1 \leqslant Z \leqslant 103$. *At. Data Nucl. Data Tables* **32**, 1 (1985).
40. Lu, H., Zhang, X., Bian, Y. & Jia, S. Topological phase transition in single crystals of $(Cd_{1-x}Zn_x)_3As_2$. *Sci. Rep.* **7**, 3148 (2017).
41. Thirupathaiah, S. *et al.* Spectroscopic evidence of topological phase transition in the three-dimensional Dirac semimetal $Cd_3(As_{1-x}P_x)_2$. *Phys. Rev. B* **98**, 085145 (2018).
42. Giannozzi, P. *et al.* QUANTUM ESPRESSO: A modular and open-source software project for quantum simulations of materials. *J. Phys. Condens. Matter* **21**, 395502 (2009).
43. Perdew, J. P., Burke, K. & Ernzerhof, M. Generalized gradient approximation made simple. *Phys. Rev. Lett.* **77**, 3865 (1996).
44. Kresse, G. & Furthmüller, J. Efficient iterative schemes for ab initio total-energy calculations using a plane-wave basis set. *Phys. Rev. B* **54**, 11169 (1996).

Acknowledgements

We thank Y. Saruta, T. Taguchi, N. Watanabe, and R. Tsubono for their assistance in the ARPES experiments. We thank K. Nagata for his assistance in the preparation of experiments. This work was supported by JST-CREST (No: JPMJCR18T1), JST-PRESTO (No: JPMJPR18L7), MEXT of Japan (Innovative Area "Topological Materials Science" JP15H05853), JSPS (JSPS KAKENHI No: JP17H01139, JP18H01160, JP19H01845, JP20H01847), Grant-in-Aid for JSPS Research Fellow (No: JP18J20058), KEK-PF (Proposal number: 2018S2-001, 2021S2-001), and UVSOR (Proposal number: 19-555, 19-841, 20-755). D.T. thanks JSPS and Tohoku University Division for Interdisciplinary Advanced Research and Education, T. Kawakami and T. Kato thank GP-Spin, for financial support.

Author contributions

The work was planned and proceeded by discussion among D.T., Y.K., K.N., S.S., T.T., K.Segawa, and T.S. K.Segawa carried out the growth of bulk single crystals and their characterization. D.T., Y.K., K.N., S.S., T.Kato, K.Sugawara, S.I., K.T., M.K., K.H., and H.K. performed the ARPES measurements. T.Kawakami, K.Y., and T.O. carried out the band calculations. D.T., Y.K., and K.N. analyzed data. D.T., Y.K., K.N., and T.S. finalized the manuscript with inputs from all the authors.

Competing interests

The authors declare no competing interests.

Additional information

Supplementary Information The online version contains supplementary material available at https://doi.org/10.1038/s41598-021-01333-z.

Correspondence and requests for materials should be addressed to K.N. or T.S.